Dalton Transactions

An international journal of inorganic chemistry

Accepted Manuscript

This article can be cited before page numbers have been issued, to do this please use: D. Wang, Y. Song, Z. Zheng, X. Zhang, Y. Wang and H. Zou, *Dalton Trans.*, 2025, DOI: 10.1039/D5DT00940E.

Volume 46
Number 10
14 March 2017
Pages 3073-3412

Dalton Transactions

An international journal of inorganic chemistry

rsc.li/dalton

ISSN 0306-0012

ROYAL SOCIETY OF CHEMISTRY

COMMUNICATION
Douglas W. Stephen *et al.*
N-Heterocyclic carbene stabilized parent sulfenyl, selenenyl, and tellurenyl cations (XH^+, X = S, Se, Te)

ROYAL SOCIETY
OF CHEMISTRY

rsc.li/dalton

View Article Online
DOI: 10.1039/D5DT00940E

One-step synthesis of Bi/C-BiOCl composites: double defect regulation, band structure modulation, visible light photocatalytic enhancement mechanism

Daoying Wang[a], Yanhua Song[a], Zhibo Zheng[a], Xiaozhen Zhang[a], Yong Wang[b*], Haifeng Zou[a*]

[a] Department of Chemical Engineering and Applied Chemistry, College of Chemistry, Jilin University, Qianjin Street 2699, Changchun 130012, P.R.China

[b] Department of Gastroenterology and Hepatology, China-Japan Union Hospital of Jilin University, Xiantai Street 126, Changchun, 130033 , P.R.China.

* haifengzou0431@sohu.com

Abstract

The treatment of large amounts of wastewater resulting from the overuse of dyes in the paper, leather and food industries is of great ecological importance. BiOCl is a promising photocatalyst due to its unique layered structure, strong chemical stability and resistance to photocorrosion. However, the advancement of photocatalytic activity was significantly impeded by the limited utilization of visible light and the elevated recombination rates of photogenerated charge carriers. Combining the defect control of semiconductor photocatalysts with Surface Plasmon Resonance (SPR) modulation can improve the efficiency of visible light conversion and photocatalysis.

Using glucose as both the carbon source and reducing agent, we successfully synthesized a BiOCl catalyst with double defect regulation (Bi/C-BiOCl) through a single-step solvothermal approach. Defect control combined with surface plasmon resonance (SPR) modulation collaboratively improves the structure and promotes photocatalytic degradation. Under simulated visible light, the Bi/C-BiOCl samples achieving a 98% degradation efficiency for 20 mg/L RhB in just 8 minutes, and the degradation rate was increased to 2.7 times that of BiOCl. The economy and simplicity of this preparation method provide a promising strategy for further exploration of high-activity BiOCl photocatalysts, this holds significant importance for the advancement of semiconductor materials in future research endeavors.

Keywords: One step synthesis; Double defect regulation; Surface plasma defect; Bi/C-BiOCl; Photocatalysis

1. Introduction

As technology and science develop by leaps and bounds, the issue of the energy crisis and environmental contamination has garnered widespread attention globally Dye is one of the most widely present contaminants in water systems, with large outputs from industrial, toxic, and difficult to biodegrade. Meanwhile, dye also has the characteristics of high COD_{Cr} value, deep color, complex composition, high content of harmful substances and difficult degradation, etc. It poses severe detrimental effects on both the ecological environment and human wellbeing. Therefore, efficient removal of dye wastewater is of great significance[1-4]. There are many common ways to treat dye

View Article Online
DOI: 10.1039/D5DT00940E

wastewater, such as adsorption[5, 6], electrochemical method[7, 8], reduction-oxidation[9, 10], photocatalysis method[11-13], etc. Among them, photocatalysis which uses clean solar energy as energy has the advantage of mild reaction conditions, no secondary pollution, and so on. Thus, it has attracted people's attention and extensive research[14]. At present, the use of semiconductor photocatalytic degradation technology to treat organic pollutants in wastewater has become a key research direction for many researchers and institutions. However, research on semiconductors with high efficiency, stability, green, and recyclability is still a core issue.

Extensive research has been conducted on bismuth-based semiconductor catalysts, attributed to their distinctive electronic configuration and excellent photocatalytic characteristics. Bismuth-based semiconductor photocatalysts, such as Bi_2MoO_6[15, 16], $(BiO)_2CO_3$[17, 18], $BiWO_6$[19, 20], Bi_2O_3[21], $BiVO_4$[22], BiOX(X=Cl、Br、I) have been reported so far[14]. They have the advantages of light corrosion resistance, good chemical stability, suitable band gap (Eg), low cost, easy preparation, stable structure, non-toxic and so on[23]. Among them, bismuth oxychloride BiOCl is a ternary semiconductor of group Ⅴ-Ⅵ-Ⅶ. Due to the interleaving of $[Bi_2O_2]^{2+}$ and Cl^- layers, the internal electric field can be formed to separate charge carriers better[18, 24-28]. Simultaneously, BiOCl's valence band is composed of O 2p and Cl 3p orbital hybridization, the Bi 6p orbitals constitute the composition of the conduction band. The structure of BiOCl featuring an indirect transition band gap can significantly suppress the recombination of photogenerated electrons and holes, so it shows excellent photocatalytic activity. From a theoretical

View Article Online
DOI: 10.1039/D5DT00940E

standpoint, a photocatalyst exhibiting a band gap width below 3.0 eV is capable of efficiently harnessing the preponderance of solar energy. [29]. However, the BiOCl bandgap value is 3.2-3.4 eV, which can only use limited ultraviolet light, and the quantum yield is low. Concurrently, the ordered surface arrangement results in a substantial rate of electron-hole pair recombination. To date, there are a lot of engineering methods have been developed to solve the above problems , including precious metal deposition[30, 31], morphological control[32, 33], heterojunction[17, 34], defect control[35] to improve the effectiveness of photocatalysts.

To broaden the visible light response spectrum further, the incorporation of metals into semiconductor photocatalysts has emerged as a proven strategy. Compared with these traditional precious metal elements (Au, Ag, Cu, etc.), the metal Bi has been found to be an inexpensive, harmless, conductive metal with advantages such as plasmon resonance (SPR) effects[36-38]. Bismuth exhibits a high Fermi level, a low density of carriers, decreased carrier quality, and an extended average free Owing to the abundance of free electrons within bismuth, path for carriers[39, 40]. Due to the presence of a large number of free electrons inside the Bi, these electrons interact with each other to form plasma. Upon excitation by incoming light, the surface electrons resonate with the incident photons at a suitable frequency, generating a localized electromagnetic field. This enables the rapid separation of photogenerated carriers.

The attributes of a negative Fermi level and a low work function in bismuth facilitate the transfer of charges between Bi metal and the semiconductor, effectively

DOI: 10.1039/D5DT00940E

inhibit electron-hole pair recombination. In the meanwhile, the non-radiative decay of the plasma can produce high-energy electrons and holes (i.e. hot charge carriers) in the metal nanostructures. High-energy hot carriers possess the capacity to stimulate surface O_2, leading to the generation of reactive oxygen species (ROS), which subsequently engage in the redox reaction. Hence, Bi serves as both a charge transfer mediator and a thermionic emitter, which significantly improves the photocatalytic activity of composites. Liu et al. used in situ reduction method to deposit element Bi on the surface of BiOCl nanosheets, Which is capable of fully decomposing 10 mg/L of MO in just 5 minutes, thereby enhancing the photocatalytic efficiency of BiOCl nanosheets, and elucidating the underlying mechanism involving bismuth[41]. However, the inefficient directional transfer of electrons in BiOCl, coupled with a high carrier recombination rate, severely hinders the subsequent transfer of injected thermal electrons to the reactants.

Defect control is an effective means to adjust the surface microstructure and electronic structure of metal oxyhalides oxides. The generation of defects affects the intrinsic electron distribution by optimizing the photoelectric properties of the photocatalyst and regulating the adsorption energy of molecules (such as H_2O, CO_2, and N_2) at the active site, regulating the adsorption energy and activation energy of molecules[42-45]. Li et al. synthesized C-doped BiOCl in a single pan using glucose as C source. Element doping and the formation of surface heterojunctions enhanced the photocatalytic activity, and the 10mg/L RhB was completely degraded within 6 min

View Article Online
DOI: 10.1039/D5DT00940E

under Xe lamp, increasing the catalytic rate by about 400%[46]. Yu et al. synthesized C-doped BiOCl by adjusting the amount of PAM, and the degradation efficiency of MO under ultraviolet light could reach 98% in 30 min[14]. Despite its intrinsically low quantum yield, the practical performance of BiOCl doped with carbon under visible light remains significantly distant from viable application. Oxygen deficiencies represent the most prevalent imperfections in semiconductor oxides. By establishing defect energy levels that effectively diminish the band gap, the recombination of photogenerated carriers can be suppressed, thereby enhancing light absorption. Additionally, these positively charged defects can serve as electron trapping centers. The oxygen vacancy is a highly active site on the surface of the oxide, which is more firmly bound to the adsorption, and has a great contribution to the reaction kinetics, and serves as a potent strategy to enhance the efficacy of the catalyst. Hou et al. used aspartic acid as a surfactant to prepare BiOCl with oxygen vacancy by modulating the pH level of the precursor solution, which could remove 80% of tetracycline hydrochloride in 1h[47]. Chen et al. employed tartaric acid as a structural directing agent to synthesize oxygen-enriched BiOCl with a narrow bandgap at ambient temperature through a one-step molecular self-assembly and recrystallization process. This method enabled the efficient degradation of 94% of RhB within a period of 20 minutes[48]. Yu et al. synthesized a novel MoO_3 material with a synergistic effect of sulfur doping and oxygen vacancies through a hydrothermal process, utilizing sulfur powder as the sulfur precursor. This material demonstrated a responsive photocurrent and remarkable cycling stability[49]. Su et al. investigated the effects of non-metallic doping and metal loading on the catalytic activity of $ZnIn_2S_4$ using first-principles methods, the results show that this method has an obvious effect on improving catalytic activity[50]0. Therefore, it is feasible to apply defect engineering and metal loading to a semiconductor to improve catalytic performance, and this methodology enhances the catalytic capability by modifying the band structure and broadening the light absorption spectrum, ultimately leading to improved photocatalytic performance.

Hence, to enhance the utilization efficiency of visible light, decrease the recombination rate of photogenerated carriers in BiOCl semiconductor materials, and augment their photocatalytic activity, we designed a Bi/C-BiOCl photocatalyst with the synergistic effect of three strategies: metal Bi loading and double defect regulation (oxygen vacancy, C-doping). Due to the weak intermolecular force of BiOCl, Bi^{3+} can be easily reduced to metal Bi in $[Bi_2O_2]^{2+}$ layer by reduction treatment. To preserve the overall charge equilibrium, some oxygen atoms from the initial lattice are ejected, resulting in the formation of oxygen vacancies[51]. As a source of C and a reducing agent, glucose can be effectively doped by regulating the amount added. Therefore, the metal Bi, oxygen vacancy and C can be introduced into BiOCl. Owing to the SPR of Bi, effect level and impurity level formed by C doping and oxygen vacancy, the prepared Bi/C-BiOCl photocatalyst showed rapid degradation of RhB under visible light, the catalytic efficiency was increased to 2.7 times of that of BiOCl, and degradation rate reached 0.44 min^{-1}, exceeding most reported BiOCl-based composites. More importantly, this catalyst can

View Article Online
DOI: 10.1039/D5DT00940E

also maintain excellent catalytic activity under strong acid conditions (pH=2), and the degradation rate is also maintained at 0.41 min^{-1}. Meanwhile, this catalyst has also demonstrated excellent degradation capabilities for other organic pollutants, such as tetracycline (TC). It is proved that this material has a wide range of application fields in degrading pollutants. This work realizes implementing three regulation strategies through a one-step synthesis, which has the advantages of simple and convenient, resource saving and environment protection. Furthermore, it offers a foundational platform for investigating enhancements in the photocatalytic properties of various semiconductor materials, thus promoting the wide application in photocatalysis.

2. Experimental procedures

2.1. Materials

The reagents utilized in this study are of analytical quality and readily obtainable from commercial sources. Bismuth nitrate ($Bi(NO_3)_3 \cdot 5H_2O$) was purchased from Mclean Biochemical, 1-octyl-3-methylimidazolium chloride ([Omim]Cl) was purchased from Lanzhou Institute of Chemical Physics, Chinese Academy of Science, Ethylene glycol (EG) was purchased from Tianjin Tiantai Chemical Co.,Ltd, Anhydrous glucose was purchased from Sinopharm Group. All chemicals were utilized directly as received, without any purification process.

2.2. Synthesis

View Article Online
DOI: 10.1039/D5DT00940E

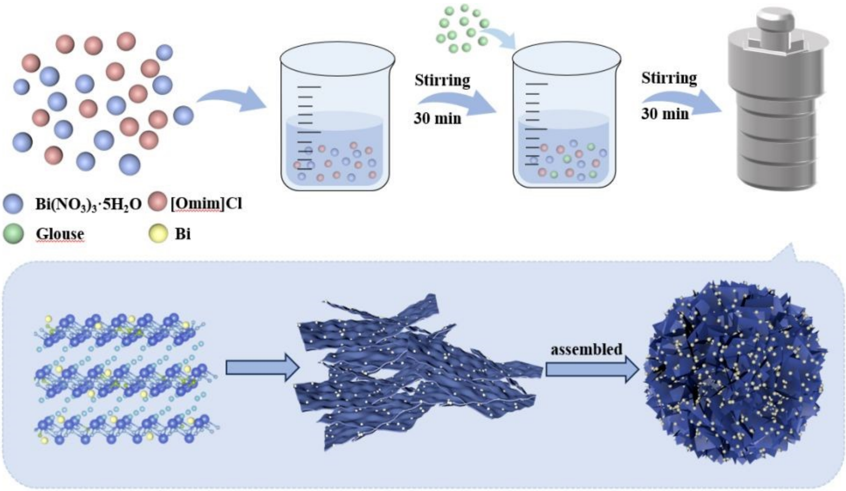

Scheme 1. Synthetic procedure diagram.

Scheme 1 shows the typical synthesis procedure of BiOCl and Bi/C-BiOCl nanosheets via the solvothermal method. 0.485 g $Bi(NO_3)_3 \cdot 5H_2O$ was dissolved in 20 mL of EG, then 0.46 g [Omim]Cl was added into the above solution and stirring continuously for 30 minutes. Then, a certain amount of anhydrous glucose was added to the previous solution and stirring for 30 minutes. The solutions were poured into 50 mL Teflon-lined autoclaves and subjected to hydrothermal treatment at a temperature of 180 °C for a duration of 12 hours. After cooling down to room temperature, the resulting precipitates were separated by washing with ethanol and deionized water 3 times and dried at 60 °C for 6 h. The final catalysts were named as Bi/C-BiOCl -1, Bi/C-BiOCl -2, Bi/C-BiOCl -3, respectively for the sample synthesized with 1, 2, and 3 mmol anhydrous glucose. The preparation process of BiOCl is alike to that of Bi/C-BiOCl but without adding anhydrous glucose on the basis of the above operation.

2.3. Characterization

View Article Online
DOI: 10.1039/D5DT00940E

The morphological characteristics of the samples were examined using scanning electron microscopy (SEM, model S-4800 from Hitachi) and transmission electron microscopy (TEM, specifically the JEM-2100 model). X-ray powder diffraction (XRD) data of the sample were recorded by Haoyuan DX-2700 X-ray diffractometer (Cu K_{α}, $\lambda = 1.5418$ Å; Voltage = 40 kV; Current = 30 mA). Brunauer-Emmett-Teller (BET) analysis was performed using a specific surface area analyzer (Micromeritics, ASAP2020HD88). An ultraviolet-visible light-near-infrared (UV-Vis-NIR) spectrophotometer (UV-4100) with an integrating sphere was used to record the ultra-violet-visible (UV-vis) reflect spectra. X-ray photoelectron spectroscopy (XPS) spectra were measured through Scanning XPS Microprobe system (Thermo Scientific K-Alpha). The Electron Spin Resonance (EPR) spectra were obtained on a Bruker E500 at room temperature. Photoelectrochemical measurements were measured on an electrochemical workstation (Chenhua, China) with a standard three electrode system of FTO glass working electrode, Pt counter electrode and Ag/AgCl electrode. The working electrode was constructed by mixing 10 mg catalyst with 0.05 and 1.00 mL nafion and ethanol solutions, and then adding the solution to the FTO region ($1*1$ cm^2) after ultrasonic treatment for 30 minutes and drying overnight in a 60℃ oven. Finally, electrochemical experiments were carried out in 0.1M Na_2SO_4 solution. Photoluminescence spectra were recorded on Horiba Jobin Yvon FluoroMax-4 fluorescence spectrophotometer using 450 W xenon lamp as light source.

2.4. Photocatalytic performance measurement

DOI: 10.1039/D5DT00940E

The photocatalytic properties of the prepared samples were evaluated by photodegradation of RhB and TC. The samples under visible light illumination, in order to assess their photocatalytic activity. We used a 300 W xenon lamp e lamp (PLS-SXE300D) as a simulated light source and a 420 nm cutoff filter.as the light source to simulate sunlight. Initially, 20 mg of catalyst were introduced into 50 mL of RhB and TC) solution, which had a concentration of 20 mg/L. The mixture was stirred in the dark for a duration of 30 minutes to attain adsorption equilibrium between the RhB (or TC) and the catalyst. Subsequently, the mixture is exposed to a xenon lamp, and every 2 minutes, 3 milliliters of the suspension are withdrawn, and a clear solution is filtered. The peak intensity was measured at 554 nm (or 357 nm) by UV-VIS spectrophotometer and the concentration of RhB (or TC) was recorded.

3. Results and discussion

3.1. Morphology and structure characterization

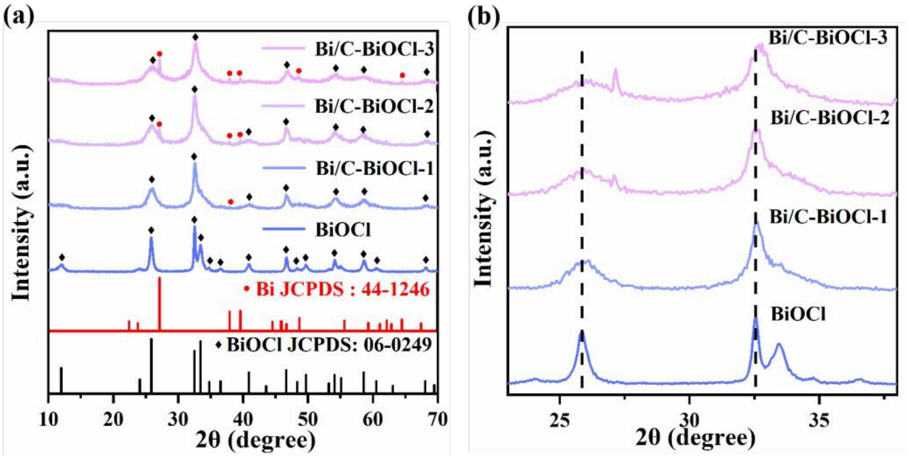

Fig. 1. (a) XRD patterns of BiOCl, Bi/C-BiOCl-1, Bi/C-BiOCl-2 and Bi/C-BiOCl-3 samples. (b) XRD amplified spectra in the range of 23°to 38°, the dash line provides a reference for the peak shifts.

View Article Online
DOI: 10.1039/D5DT00940E

In order to better understand the structure and phase purity of the prepared BiOCl series samples, XRD test was performed. Fig. 1(a) shows the XRD pattern of a series of synthesized samples. The diffraction peaks observed for the single-phase BiOCl align well with the reference XRD pattern corresponding to BiOCl (JCPDS NO. 06-0249), and no other impurities are detected. With the addition of anhydrous glucose, the peaks of BiOCl were weakened, and obvious metallic Bi peaks appeared at 2θ = 27.2°, 37.9°, 39.6°, 48.7°, 64.5°, corresponding to the crystal plane of (012), (104), (110), (202) and (122) of Bi (JCPDS NO. 44-1246). At the same time, compared with BiOCl, the half-maximum width of the XRD peak of Bi/C-BiOCl increased, and the addition of glucose led to the decrease of crystal size and anisotropy growth. Fig. 1(b) shows a locally enlarged view of the characteristic peaks between 23.0° and 38.0°. The diffraction peaks in Bi/C-BiOCl were observed to shift slightly to higher angles, which can be attributed to lattice contraction caused by carbon incorporation, and also confirmed that C doping concentration increases with the increase of anhydrous glucose dosage.

View Article Online
DOI: 10.1039/D5DT00940E

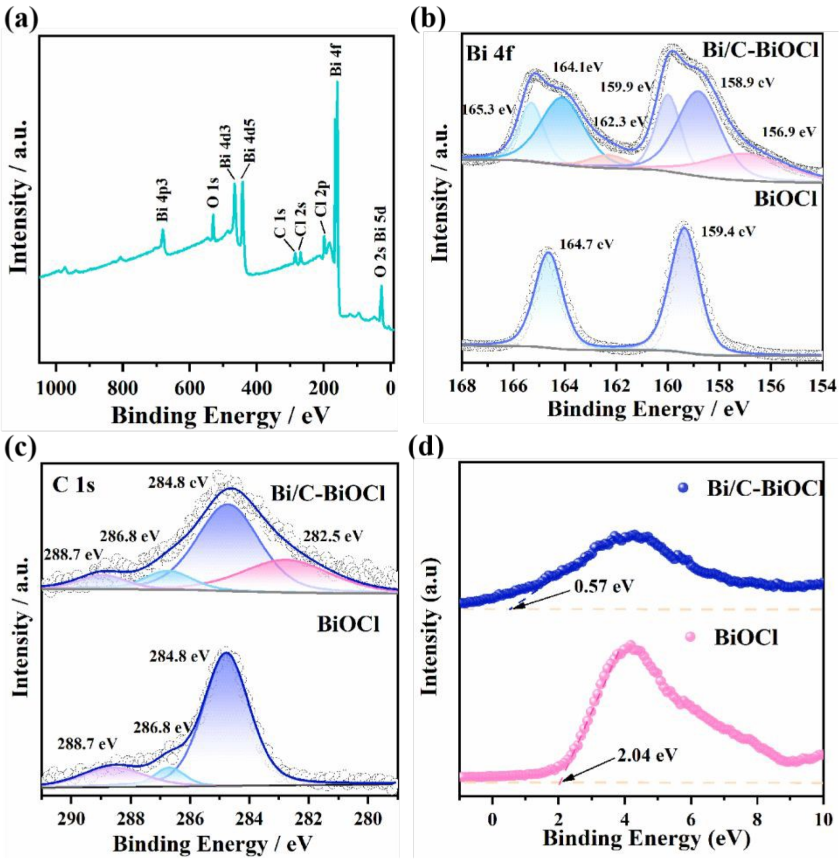

Fig.2. The XPS spectra (a), high resolution Bi 4f (b), C 1s (c), and valence band (VB) (d) of BiOCl and Bi/C-BiOCl.

To further investigate its chemical composition and valence states, XPS analysis was employed, and the effects of C doping and Bi elemental loading on BiOCl structure were discussed. From Fig. 2(a), an intuitive analysis reveals that Bi/C-BiOCl consists of Bi, O, Cl, and C elements, with no other impurities present. Fig. 2(b) shows the typical peaks of Bi^{3+} are observed at 159.4 eV and 164.7 eV, which correspond to Bi $4f_{7/2}$ and Bi $4f_{5/2}$, respectively[52]. The peaks located at 158.9 eV and 164.1 eV are assigned to the Bi^{3+} in a lower oxidation state, which may result from the bonding between carbon and Bi[53]. The peaks characteristic of Bi^0 emerge at 156.9 eV and 162.3 eV, which are associated with Bi $4f_{7/2}$ and Bi $4f_{5/2}$, respectively. This finding indicates

View Article Online
DOI: 10.1039/D5DT00940E

the presence of bismuth (Bi) elemental species on the surface of the Bi/C-BiOCl layer, aligning with the results obtained from XRD analysis[54]. It is crucial to highlight that following C doping and Bi loading, the two peaks associated with Bi $4f_{7/2}$ and Bi $4f_{5/2}$ exhibit a positive shift in chemical binding energy, suggesting that electrons on the surface tend to migrate from the C-BiOCl layer towards the Bi species present on the surface. Fig. 2(c) presents the high-resolution spectra of C1s for the Bi/C-BiOCl composite. C-C (284.8 eV) was used as the basis for charge correction. Peaks at 286.8 eV and 288.6 eV are attributed to C-O-C and O-C=C extraneous pollution C, respectively. The C-Bi bond signal in Bi/C-BiOCl appears at 282.5 eV, exhibiting the C dopant successfully to the BiOCl lattice to form C-Bi bonds[55]. This is consistent with XRD analysis. Observing Figure. 2(d), it is evident that the distances from the maximum valence band to the Fermi level, as determined by VB-XPS spectra, range from 2.04 eV to 0.57 eV. Generally speaking, the greater the valence band value, the stronger the oxidation capacity of the sample.

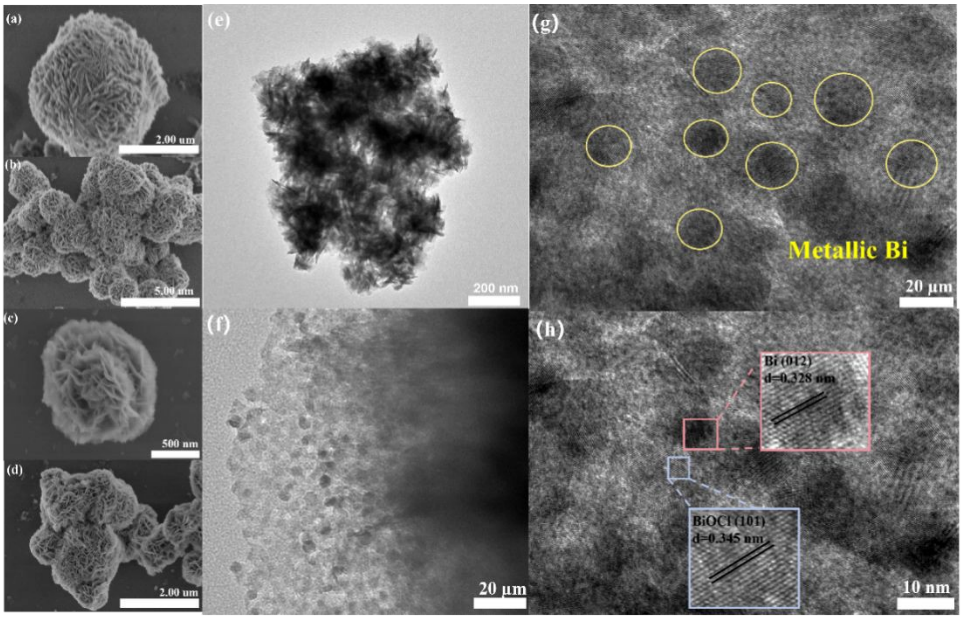

View Article Online
DOI: 10.1039/D5DT00940E

Fig.3. SEM images of (a, b) BiOCl and (c, d) Bi/C-BiOCl, (e-h) TEM and HRTEM images of Bi/C-BiOCl.

Fig. 3 indicates the SEM and TEM images of BiOCl and Bi/C-BiOCl microspheres assembled from nanosheets. From Fig. 3(a-d), BiOCl and Bi/C-BiOCl have diameters of 1.25 μm and 0.85 μm, respectively. In comparison to BiOCl, the particle size of Bi/C-BiOCl is significantly reduced, this leads to an increased specific surface area and a greater number of active catalytic sites, thus enhancing the adsorption and degradation ability. The sheet thickness of BiOCl is 0.04 μm, the thickness of Bi/C-BiOCl medium sheet is reduced to 0.02 μm, and the binding of the pieces is looser than that of BiOCl. Generally speaking, a thinner sample results in a shorter electron migration distance, thereby suppressing the recombination of photogenerated carriers and enhancing the catalytic rate. The TEM image depicted in Figure. 3(e-h) reveals that Bi/C-BiOCl consists of nanosheets adorned with numerous particles on their surfaces. In Fig. 3(g), it is evident that metal Bi nanodots are evenly distributed across the surface of the BiOCl nanosheets. In Fig. 3(h), distinct lattice fringes of 0.328 nm and 0.345 nm can be clearly observed, which are consistent with the (012) crystal face of Bi and the (101) crystal face of BiOCl, respectively. Collectively, these findings suggest that the direct loading of Bi onto BiOCl.

View Article Online
DOI: 10.1039/D5DT00940E

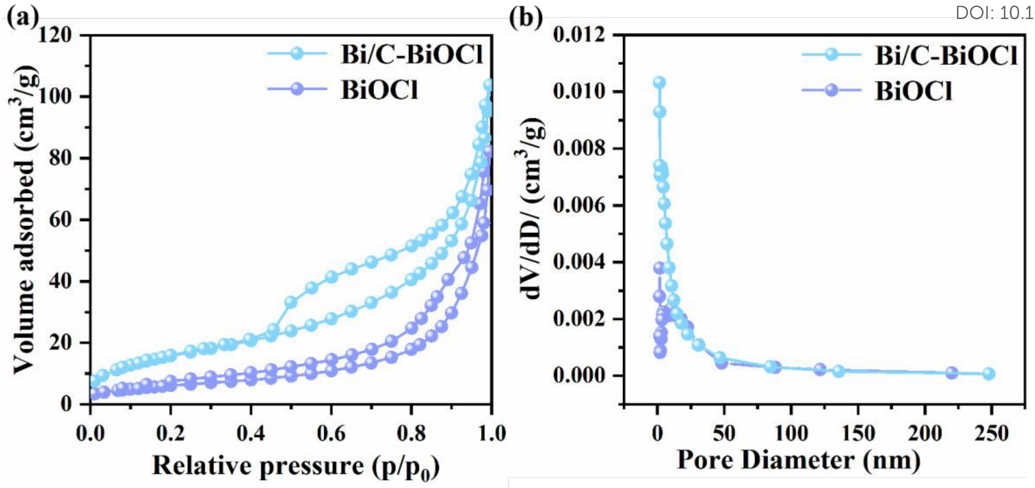

Fig.4. (a) N_2 adsorption-desorption isotherms and (b) BJH pore size distribution curves.

The microstructure of materials can also be effectively characterized by their specific surface area. As shown in Fig. 4, the N_2 adsorption/desorption isotherms of BiOCl and Bi/C-BiOCl were measured to determine their specific surface area and the pore size distributions. As depicted in Fig. 4(a), the N_2 adsorption/desorption isotherms of BiOCl and Bi/C-BiOCl exhibited typical Ⅳ and type H3 hysteresis isotherms, which are slit pores generated by the accumulation of sheet particles, indicating the presence of mesoporous structures in the samples[56]. The specific surface areas of BiOCl and Bi/C-BiOCl were 22.48 m^2g^{-1} and 58.26 m^2g^{-1}, respectively. The specific surface area of Bi/C-BiOCl is increased to 2.6 times that of BiOCl, which is due to the hindered crystallization of Bi/C-BiOCl induced by C doping[57]. A larger specific surface area favors the adsorption of pollutants by the photocatalyst. Fig 4. (b) shows the aperture distribution curves of BiOCl and Bi/C-BiOCl. BiOCl and Bi/C-BiOCl have average pore sizes of 11.0 nm and 22.6 nm, respectively. Based on the IUPAC classification,

View Article Online
DOI: 10.1039/D5DT00940E

both BiOCl and Bi/C-BiOCl possess pore sizes that categorize them as mesoporous materials. This pore size classification aligns with the observed N_2 adsorption/desorption isotherms.

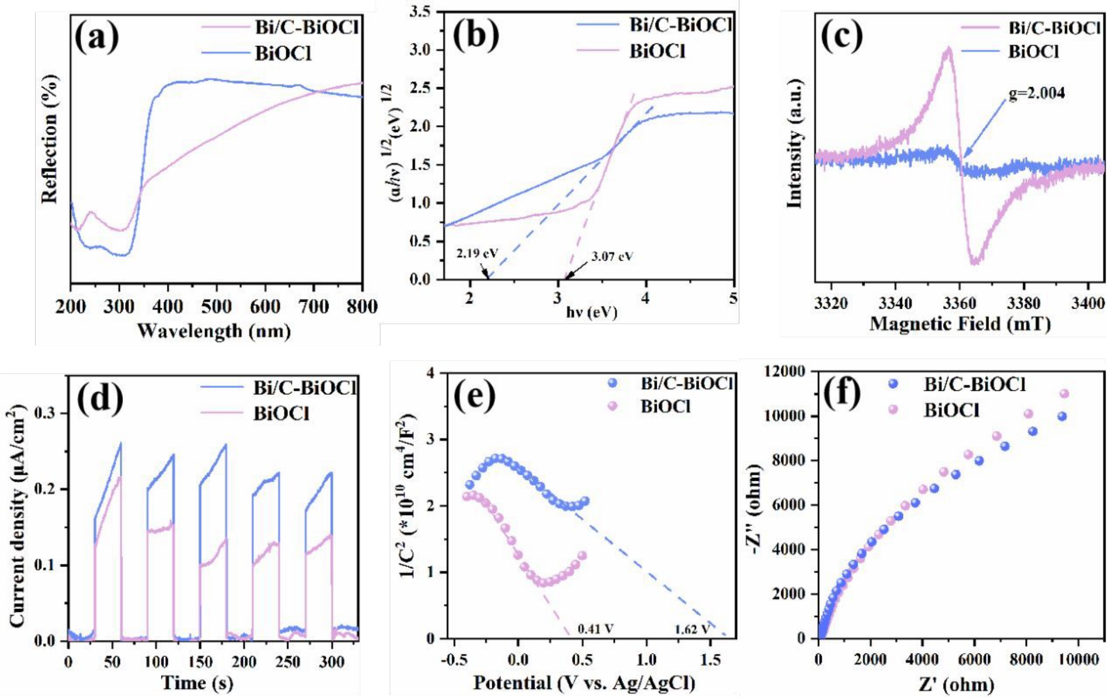

Fig.5. (a) UV-VIS diffuse reflectance spectra; (b) Tauc plots; (c) EPR spectra; (d) transient photocurrent response of samples; (e) Mott-Schottky plot and (f) EIS Nyquist plots of the photocatalysts.

The findings related to pore sizes were in agreement with the outcomes obtained from the N_2 adsorption/desorption isotherms. Compared with BiOCl, Bi/C-BiOCl has larger specific surface area and pore size, expose more active sites, which can significantly improve the photocatalytic charge transfer[58].

By analyzing the UV-Vis diffuse reflectance spectra of the sample, the spectral region within which the sample absorbs light can be determined. As depicted in Figure. 5(a), the absorption edge for BiOCl samples is approximately 370 nm, while the

View Article Online
DOI: 10.1039/D5DT00940E

adsorption edge is redshifted after C doping and Bi loading, extending to 700 nm, this suggests a reduced band gap and an expanded response to visible light. The application performance of a semiconductor is significantly influenced by its band gap value, as is well-established. The bandgap values (Eg) of as-prepared samples were calculated by the Kubelka-MunK equation[59]:

$$F(R) = \frac{(1-R)^2}{2R}$$

(1)

$$[F(R)*h\upsilon]^{1/2} = A(h\upsilon - Eg) \qquad (2)$$

where R presents the reflectance, h is Planck's constant, υ is frequency. Band gap energy diagram was plotted with Eg (Eg=hυ) and $[F(R)*h\upsilon]^{1/2}$ as horizontal and vertical coordinates, respectively. The bandgap values obtained through calculation are presented in Figure. 4(b). The band gap for BiOCl measures 3.07 eV, whereas for Bi/C-BiOCl, it is decreased to 2.19 eV. The doping of non-metallic C will form an impurity energy level below the BiOCl conduction band, and reduce the band gap to enhance the absorption and utilization of visible light. Furthermore, a notable alteration in the catalyst's coloration is observed. Pure BiOCl exhibits a pristine white hue, whereas Bi/C-BiOCl displays a considerably darker brown shade compared to BiOCl. This color modification arises due to the incorporation of oxygen vacancies, leading to the creation of defect levels beneath the conduction band and suppressing the rate of photogenerated carrier recombination[60]. The combined influence of the two factors led to a reduction in the band gap value and an enhancement in the photocatalytic activity of the sample.

View Article Online
DOI: 10.1039/D5DT00940E

Electron paramagnetic resonance spectroscopy (EPR) is an effective means to detect the presence of defects, the existence of oxygen vacancies was further verified by testing EPR. As shown in Fig. 5(c), clear paramagnetic signals are displayed for Bi/C-BiOCl and BiOCl and g=2.004, the EPR signal intensity of Bi/C-BiOCl is notably higher compared to that of BiOCl. that the oxygen vacancy concentration in Bi/C-BiOCl is higher. Previous work has shown that semiconductors incorporating oxygen vacancies can markedly improve the efficiency of electron-hole separation and expedite the photocatalytic reaction[61]. Fig. 5(d) shows the transient photocurrent curve at room temperature. It is evident that, in comparison to BiOCl, Bi/C-BiOCl has a stronger photocurrent response, the separation efficiency of photogenetic-electron holes is higher, and almost no photocurrent density attenuation is observed, which also indicates that Bi/C-BiOCl has excellent photostability[51]. The X-intercepts depicted in Fig. 5(e) represent the flat-band potentials for BiOCl and Bi/C-BiOCl, yielding values of 0.41V and 1.62V, respectively. Generally speaking, the valence band potential of P-type semiconductors exceeds the flat-band potential by approximately 0.2V (relative to the NHE). As shown in the Fig. 5(e), the flat-band potential is the X-intercept of BiOCl and Bi/C-BiOCl, which are 0.41 and 1.62V, respectively. In general, the valence band potential of P-type semiconductors is about 0.2 V positive (relative to NHE) than the flat band potential. The test potential (Vs. Ag/AgCl) was converted to a reversible hydrogen electrode (E_{RHE}) according to the NERNST equation:

View Article Online
DOI: 10.1039/D5DT00940E

$E(vs.\ \mathrm{RHE}) = E(vs. Ag/AgCl) + E_{\mathrm{Ag/AgCl}}(reference) + 0.059 \times pH$

(3)

$E_{CB} = E_{VB} - E_g$

(4)

where E_{RHE} is the conversion potential to RHE and $E_{\mathrm{Ag/AgCl}}$ represents the experimental result to Ag/AgCl, $E_{\mathrm{Ag/AgCl}}$ (reference) is 0.197 V at 25℃. Calculated by formula 3, the VB positions of BiOCl and Bi/C-BiOCl are 1.22 and 2.43 V, and depending on the band gap width, the complete reversible hydrogen electrode (RHE) can be calculated by formula 4. Their CB were -1.85 and 0.24 V. The electrochemical impedance spectroscopy (EIS) technique was employed to assess the photoelectric properties of BiOCl and Bi/C-BiOCl. It is widely accepted that a decreased arc radius indicates a lower charge transfer resistance, thereby facilitating the more rapid separation of photogenerated charges. In comparison to BiOCl, Bi/C-BiOCl exhibits a lower resistance to charge transfer. Combining above results, the prepared Bi/C-BiOCl exhibits excellent photoelectric properties, this can be ascribed to the combined influence of defect modulation and the surface plasmon resonance (SPR) effect. Moreover, the higher PL intensity implies a higher electron-hole recombination ratio, which often corresponds to a decrease in photocatalytic activity[62]. According to Fig. S1, the PL intensity of Bi/C-BiOCl is much lower than that of BiOCl. This indicates that the combination of the three strategies of oxygen vacancies, Bi metal loading and C element doping are conducive to rapid charge transfer.

3.2 Photocatalytic degradation of RhB

3.2.1. Photocatalytic performance evaluation

View Article Online
DOI: 10.1039/D5DT00940E

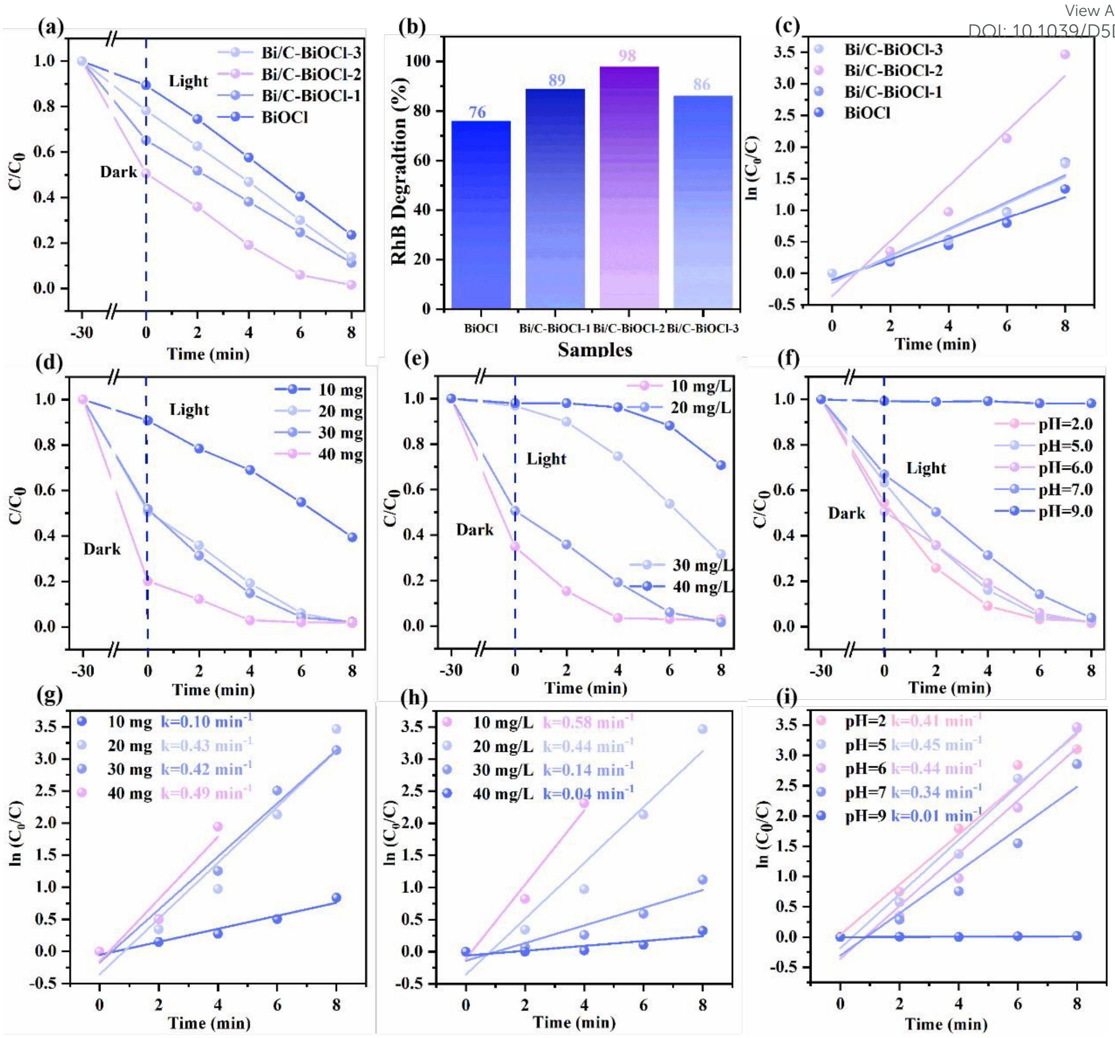

Fig.6. (a) Visible light-driven photocatalytic performance of RhB on serious Bi/C-BiOCl; (b) degradation efficiency of RhB; (c) kinetic profiles of the reaction; (d, g) the effect of varying catalyst loading on the degradation of RhB and its corresponding kinetic behavior; (e, h) the impact of initial RhB concentration on its degradation process and the corresponding kinetic parameters; and (f, i) effect of different pH and corresponding kinetics.

The photocatalyst Bi/C-BiOCl, synthesized through the combined influence of Bi-induced oxygen deficiency and carbon doping, demonstrates remarkable photocatalytic performance. Under xenon lamp illumination, the photocatalytic degradation of RhB

View Article Online
DOI: 10.1039/D5DT00940E

was initiated through the addition of the photocatalyst. Fig. 6(a) shows the photocatalytic degradation rate of RhB by Bi/C-BiOCl series samples. Considering about the above facts, we can conclude that the surface adsorption performance of RhB is significantly improved compared with that of BOC samples. When no glucose was added, the adsorption rate of BiOCl to RhB was 12%. The adsorption rates of RhB were increased to 36%, 48% and 22%, respectively. The surface adsorption performance of Bi/C-BiOCl was significantly improved compared with that of BiOCl samples, and the reason for the more than 4-fold increase in the adsorption performance of Bi/C-BiOCl-2 can be ascribed to its expanded specific surface area and the more porous sheet structure, which in turn augment the number of active sites and the contact interface with contaminants. In addition, the vacancy-induced charge difference distribution enhances the interaction between vacancies and adsorbed molecules, and reduces the adsorption energy and activation energy. Hence, there has been a notable enhancement in the adsorption efficacy of Bi/C-BiOCl-2. After 8 min irradiation by xenon lamp, the degradation rate of BiOCl nanosheets to 20mg/L RhB was 76%. While the degradation rates of Bi/C-BiOCl-1, Bi/C-BiOCl-2 and Bi/C-BiOCl-3 series samples were increased to 89%, 99% and 86%, respectively. This trend is consistent with the adsorption properties. As shown in Fig. 6(c), the observed reaction rate constant, designated as K, for the degradation of BiOCl is 0.16 min^{-1}, and that for Bi/C-BiOCl-1, Bi/C-BiOCl-2 and Bi/C-BiOCl-3 was 0.21, 0.44, 0.21 min^{-1}, respectively. The Bi/C-BiOCl-2 sample prepared exhibited an almost 2.7-fold increase in performance compared to BiOCl.

Additionally, it is evident that the degradation rate of RhB in the synthesized Bi/C-BiOCl series samples has undergone enhancement when compared to BiOCl, showing a trend of first increasing and then decreasing. This is because as the amount of glucose increases, Bi^{3+} in the BiOCl lattice is reduced to larger Bi elements, reducing the active site on the Bi/C-BiOCl surface and reducing photocatalytic activity. And the error analysis of the degradation of RhB by Bi/C-BiOCl-2 under visible light was conducted as shown in Fig. S2. It can be found that the length of the error bar is appropriate, which can confirm the credibility of the excellent degradation ability of the catalyst for RhB.

3.2.2. The impact of catalyst dosage

Take into account the economic implications of catalyst dosage during practical wastewater treatment processes. As depicted in Figure 6(d), an assessment of the removal efficiency of Bi/C-BiOCl was conducted for various catalyst dosages when the initial RhB concentration was set at 20 mg/L. Upon increasing the catalyst dosage from 10 mg to 20 mg, the removal rate showed a significant surge from 61% to 98%. Meanwhile, as shown in Fig. 6(g), the K was increased by 4.3 times compared with 10 mg (0.10 min^{-1}) when the addition amount of Bi/C-BiOCl was 20 mg (0.43 min^{-1}), and the degradation rate could reach 98% in 8 min. The primary reason for the improvement in RhB degradation is the increased dosage of Bi/C-BiOCl, resulting in a higher number of active sites and a larger total surface area, which in turn boosts the adsorption capacity. Upon raising the catalyst quantity to 30 mg and 40 mg, the degradation rate and removal rate basically remained unchanged, which was mainly due to the increase

View Article Online
DOI: 10.1039/D5DT00940E

of the amount of Bi/C-BiOCl. The augmentation in the number of active sites and total surface area, coupled with an enhanced adsorption capacity, led to a notable improvement in the RhB degradation efficiency. When the adsorption capacity and activity potential can satisfy the adsorption and activation of RhB molecules, an increase in the Bi/C-BiOCl input did not exert a notable influence on the degradation of RhB in aqueous solution. In addition, after dark stirring, the concentration of RhB appeared the same rule. Therefore, considering the economy and cost in practical applications, the optimal addition amount of catalyst is 20mg.

3.2.3. The impact of contaminant density

Fig. 6(e) lustrates the influence of varying initial concentrations of RhB, ranging from 10 to 40 mg/L, on the efficiency of removal by Bi-C/BiOCl composites. As the RhB concentration rose to 30 mg/L and further to 40 mg/L, there was a notable decline in the RhB removal rate, decreasing from 98% to 68% and subsequently to 29%, indicating that the removal effect of RhB at high concentrations would be correspondingly reduced. This occurrence is attributed to the fact that, at elevated RhB concentrations, a significant portion of the active surface sites becomes occupied by RhB molecules[51].

3.2.4. The impact of pH

The pH level of the solution at the outset modifies the surface charge characteristics and electrostatic interactions of the catalyst, thereby exerting a particular effect on the photocatalytic degradation rate. When the RhB concentration is initially

View Article Online
DOI: 10.1039/D5DT00940E

set to 20 mg/L and a catalyst quantity of 20 mg is introduced, the photocatalytic efficiency of Bi/C-BiOCl was evaluated when pH of RhB was 2.0, 5.0, 6.0, 7.0, 9.0. According to Fig. 6(f, i), the removal rates of RhB by Bi/C-BiOCl at different pH values were 98%, 98%,98%, 96% and 1.8%, respectively. At a solution pH of 5.0, the removal rate of RhB was the highest, and the overall difference of degradation efficiency and catalytic activity was small in the range of 2.0-7.0, indicating that Bi/C-BiOCl had comprehensive photocatalytic activity under both acidic and neutral conditions. Nonetheless, as the pH continues to rise, the degradation rate undergoes a gradual decline, particularly in alkaline conditions, resulting in a significant reduction in photocatalytic activity. This is due to the fact that, at elevated pH levels, the solution contains a higher concentration of hydroxide ions, leading to competition with RhB molecules for active sites and consequently decreasing the degradation efficiency[51]. Therefore, Bi/C-BiOCl showed good photocatalytic activity in the range of pH=2.0-7.0, which was suitable for sewage treatment in practice.

3.3. Degradation of other pollutants

In addition, the degradation ability of Bi/C-BiOCl for TC was also tested, as shown in Fig.S3. It can be concluded that compared with BiOCl, Bi/C-BiOCl shows more excellent adsorption and visible light degradation capabilities, suggesting that the photocatalyst developed in this study has substantial potential for practical applications.

3.4. Free radical capture and recycling stability of catalyst

View Article Online
DOI: 10.1039/D5DT00940E

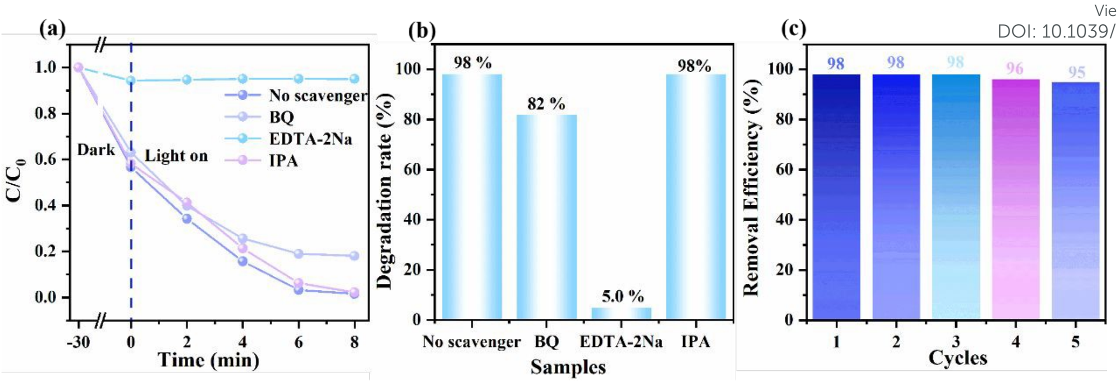

Fig.7. (a) Impact of varied capturing agents on the degradation process of RhB; (b) photodegradation efficiency of different trapping agents on RhB; (c) degradation cycles of RhB.

To gain deeper insights into the photocatalytic removal mechanism of RhB, experiments involving radical scavengers were conducted, aiming to investigate the radicals produced during the photocatalytic degradation process of the samples. During this experimental series, EDTA-2Na, IPA and BQ served as scavengers to selectively capture the generated h^+, $\cdot OH$ and $\cdot O_2^-$, respectively. After the application of various scavengers, the degree of RhB removal decreased to varying extents. As indicated in Fig. 7(a, b), the RhB removal efficiency diminished to 5.0% upon the addition of EDTA-2Na, whereas it decreased to 82% after incorporating BQ. Moreover, when IPA was added, there was little change in the removal efficiency of RhB and no change in the photocatalytic degradation effect. Therefore, in the photodegradation of RhB catalyzed by Bi/C-BiOCl, h^+ plays a predominant role, whereas $\cdot O_2^-$ has a lesser but significant impact, and $\cdot OH$ contributes negligibly to the degradation process. Assessing the practical applicability of the catalyst hinges on its reusability, prompting further testing of the stability of Bi/C-BiOCl. As illustrated in Figure 7(c), following

View Article Online
DOI: 10.1039/D5DT00940E

five cycles, the degradation performance of Bi/C-BiOCl exhibited a minor decline, yet it consistently maintained an efficiency above 95%. The decrease in price reduction efficiency can be attributed to the loss of catalysts during use and separation. And the samples after circulation were characterized by XRD and SEM. Evidently, Fig. 4S. (a) shows the XRD results, no additional diffraction peaks are observed in the recycled catalyst, but only a slight decrease in crystallinity. This may be due to the adsorption of intermediates and by-products on the surface of the photocatalyst during the degradation process. Likewise, Fig. 4S. (b) shows the morphology of samples also remained intact. All the results confirm the excellent stability and durability of Bi/C-BiOCl.

3.5. Compare with other jobs

Compared with BiOCl photocatalysts prepared previously, Bi/C-BiOCl prepared in this work showed good degradation activity, as shown in Table 1[19, 46, 60, 63-68]. The Bi/C-BiOCl photocatalyst showed the fastest catalytic rate and the best degradation effect with the least amount of addition, which confirmed the great application prospect of this work.

View Article Online
DOI: 10.1039/D5DT00940E

Table 1 Comparison of RhB photodegradation with BiOCl-based photocatalysts reported in the literature.

Sample	Concentration	Quality of catalyst	Reaction time	Degradation rate	k (min^{-1})	Ref.
BiOCl	20 mg/L	50 mg	140 min	90.00 %	0.0134	[63]
BiOCl	20 mg/L	20 mg	120 min	100 %	0.0451	[64]
Bi/BiOCl	25 mg/L	50 mg	120 min	99.40 %	0.0223	[65]
Bi@BiOCl	10 mg/L	25 mg	50 min	100 %	none	[66]
Bi/BiOCl	20 mg/L	100 mg	120 min	98.90 %	none	[60]
C-BiOCl	20 mg/L	50 mg	10 min	95.00 %	none	[46]
FOD-ore	20 mg/L	50 mg	90 min	85 %	0.017	[69]
T-100-V_O	10 mg/L	50 mg	30 min	96.8 %	0.097	[67]
Bi/C-BiOCl	**20 mg/L**	**20 mg**	**8 min**	**98.43 %**	**0.4360**	**This work**

3.6. Degradation pathways

Considering the preceding discussion, a tentative photocatalytic mechanism is illustrated in Figure. 8. Upon excitation by incident light, Bi/C-BiOCl undergoes a process influenced by the surface plasmon resonance of Bi, the metal Bi can efficiently convert solar energy into thermal electrons and heat to drive chemical reactions, and the generated high-energy electrons can be excited and transferred to conductive bands similar to semiconductors to participate in the valence band. Since the doping of the C element creates impurity levels, electrons located in the valence band can readily

View Article Online
DOI: 10.1039/D5DT00940E

transition to the conduction band, necessitating minimal energy input. The excited electrons that transition from the valence band are captured by oxygen vacancies that act as electrons traps and are prevented from recombining with the light-induced holes that from simultaneously in the valence band.

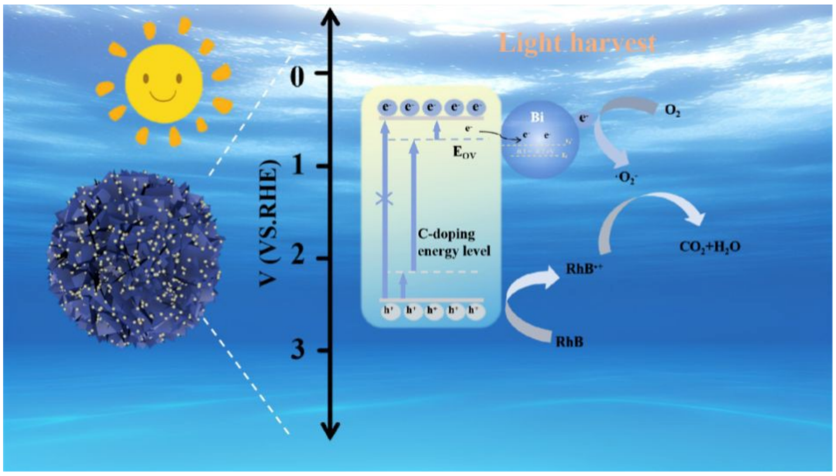

Fig.8. A plausible mechanism for the adsorption-photocatalytic degradation facilitated by Bi/C-BiOCl.

An oxygen vacancy facilitates a transition process, capturing electrons from the valence band. Subsequently, these trapped electrons can readily transfer from the valence band to the conduction band, demanding only a minimal amount of energy. Serving as an electron trap, the oxygen vacancy temporarily holds onto the excited electrons, thereby reducing the likelihood of their recombination with the concurrently formed light-induced holes in the valence band. Electrons are further transferred to nearby Bi nanoparticles that act as metal electron acceptors. Following this, the electrons are subsequently relayed to adjacent Bi nanoparticles, functioning as metallic electron sinks, and engage in the photocatalytic reaction, resulting in the decomposition of RhB into smaller molecules, including CO_2 and H_2O. Furthermore, oxygen

View Article Online
DOI: 10.1039/D5DT00940E

molecules are adsorbed onto the OVs sites and undergo activation via the localized electronic states arising from the presence of Ovs, further promoting the degradation of organic pollutants into non-toxic small molecules, CO_2, and H_2O.

4. Conclusions

In this paper, the Bi/C-BiOCl light catalyst was synthesized through the solvent thermal method using glucose as the C source and reducing agent, and the synergistic regulation of the two-defect regulation and SPR effect was realized. Thin nanosheets, possessing a thickness of approximately 2μm, were assembled into 3D flower-like structures, characterized by a high specific surface area and an interwoven mesoporous architecture, which provided good adsorption capacity for dye degradation and a large number of active sites. Hence, it facilitated the adsorption and decomposition of pollutants effectively. The thinner nanosheets shorten the migration distance of electrons and electron-hole pair recombination is obviously hindered during the migration process, which is advantageous to the photocatalytic reaction. C doping and the presence of oxygen vacancy form impurity levels and defect levels above valence the and below the conduction band. Compared with BiOCl, the band gap is reduced to 2.19 eV and the light absorption range is widen. Under visible light illumination, a degradation efficiency of 98% was achieved for 20 mg/L RhB within 8 minutes, demonstrating remarkable photocatalytic efficacy. This method can effectively improve the band structure, enhance the effectiveness of visible light utilization, the

DOI: 10.1039/D5DT00940E

surface electron concentration and the active site, effectively inhibit the photogenerated carrier recombination ability, and improve the visible light degradation ability of the catalyst. This provides a new approach for the optimization of Bi-based materials, while providing a new perspective and strategy that can be extended to other semiconductor materials.

Acknowledgements

This work was financially supported by the National Natural Science Foundation of China (Grant No. 52073120).

Data Availability Statement

The data that support the findings of this study are available on request from the corresponding authors.

References

1. A. Rafiq, M. Ikram, S. Ali, F. Niaz, M. Khan, Q. Khan and M. Maqbool, *Journal of Industrial and Engineering Chemistry*, 2021, **97**, 111-128.
2. M. Arami, N. Limaee, N. Mahmoodi and N. Tabrizi, *Journal of Hazardous Materials*, 2006, **135**, 171-179.
3. A. El Nemr, E. T. Helmy, E. A. Gomaa, S. Eldafrawy and M. Mousa, *Journal of Environmental Chemical Engineering*, 2019, **7**.
4. L. Aljerf, *Journal of Environmental Management*, 2018, **225**, 120-132.
5. J. Cao, Z.-h. Yang, W.-p. Xiong, Y.-y. Zhou, Y.-r. Peng, X. Li, C.-y. Zhou, R. Xu and Y.-r. Zhang, *Chemical Engineering Journal*, 2018, **353**, 126-137.
6. Z. Li, Y. Sun, J. Xing, Y. Xing and A. Meng, *Journal of Hazardous Materials*, 2018, **352**, 204-214.
7. X. Peng, J. Cao, B. Xie, M. Duan and J. Zhao, *Ecotoxicology and Environmental Safety*, 2020, **188**.
8. I. Yahiaoui, F. Aissani-Benissad, F. Fourcade and A. Amrane, *Chemical Engineering Journal*, 2013, **221**, 418-425.

9. J. Duan, L. Bai, K. Xu, Q. Fang, Y. Sun, H. Xu, K. C.-F. Leung and S. Xuan, *Journal of Hazardous Materials*, 2020, **384**.
10. Q. Fang, J. Zhang, L. Bai, J. Duan, H. Xu, K. Cham-Fai Leung and S. Xuan, *Journal of Hazardous Materials*, 2019, **367**, 15-25.
11. Q. Zhu, Y. Sun, F. Na, J. Wei, S. Xu, Y. Li and F. Guo, *Applied Catalysis B: Environmental*, 2019, **254**, 541-550.
12. Y. Lu, Y. Chu, W. Zheng, M. Huo, H. Huo, J. Qu, H. Yu and Y. Zhao, *Electrochimica Acta*, 2019, **320**.
13. Q. Zhang, J. Bai, G. Li and C. Li, *Journal of Solid State Chemistry*, 2019, **270**, 129-134.
14. J. Yu, B. Wei, L. Zhu, H. Gao, W. Sun and L. Xu, *Applied Surface Science*, 2013, **284**, 497-502.
15. L. Zhang, T. Xu, X. Zhao and Y. Zhu, *Applied Catalysis B: Environmental*, 2010, **98**, 138-146.
16. J. Bi, L. Wu, J. Li, Z. Li, X. Wang and X. Fu, *Acta Materialia*, 2007, **55**, 4699-4705.
17. M. Long, P. Hu, H. Wu, J. Cai, B. Tan and B. Zhou, *Applied Catalysis B: Environmental*, 2016, **184**, 20-27.
18. H. Cheng, B. Huang, K. Yang, Z. Wang, X. Qin, X. Zhang and Y. Dai, *ChemPhysChem*, 2010, **11**, 2167-2173.
19. Z. Jiang, X. Liang, H. Zheng, Y. Liu, Z. Wang, P. Wang, X. Zhang, X. Qin, Y. Dai, M.-H. Whangbo and B. Huang, *Applied Catalysis B: Environmental*, 2017, **219**, 209-215.
20. C. Li, G. Chen, J. Sun, J. Rao, Z. Han, Y. Hu, W. Xing and C. Zhang, *Applied Catalysis B: Environmental*, 2016, **188**, 39-47.
21. L. Zhang, W. Wang, J. Yang, Z. Chen, W. Zhang, L. Zhou and S. Liu, *Applied Catalysis A: General*, 2006, **308**, 105-110.
22. M. A, M. J, M. Ashokkumar and P. Arunachalam, *Applied Catalysis A: General*, 2018, **555**, 47-74.
23. C. T. Haile, K. H. Ng, C.-W. Chiu, N. Ahmad and C.-F. J. Kuo, *Materials Today Physics*, 2024, **42**.
24. W. Wang, F. Huang and X. Lin, *Scripta Materialia*, 2007, **56**, 669-672.
25. S. Shenawi-Khalil, V. Uvarov, Y. Kritsman, E. Menes, I. Popov and Y. Sasson, *Catalysis Communications*, 2011, **12**, 1136-1141.
26. T. Saison, N. Chemin, C. Chanéac, O. Durupthy, V. Ruaux, L. Mariey, F. Maugé, P. Beaunier and J.-P. Jolivet, *The Journal of Physical Chemistry C*, 2011, **115**, 5657-5666.
27. J. Krishna Reddy, B. Srinivas, V. Durga Kumari and M. Subrahmanyam, *ChemCatChem*, 2009, **1**, 492-496.
28. W. Yin, W. Wang, L. Zhou, S. Sun and L. Zhang, *Journal of Hazardous Materials*, 2010, **173**, 194-199.
29. R. P. Barkul, V. B. Koli, V. B. Shewale, M. K. Patil and S. D. Delekar, *Materials*

View Article Online
DOI: 10.1039/D5DT00940E

Chemistry and Physics, 2016, **173**, 42-51.

30. P.-A. Hsieh, P.-J. Chen, L.-M. Lyu, S.-Y. Chen, M.-C. Tseng, M.-Y. Chung, W.-H. Chiang, J.-L. Chen and C.-H. Kuo, *ACS Applied Materials & Interfaces*, 2021, **13**, 58799-58808.
31. A. Kuila, P. Saravanan, D. Bahnemann and C. Wang, *Applied Catalysis B: Environmental*, 2021, **293**.
32. S. Wu, C. Wang, Y. Cui, T. Wang, B. Huang, X. Zhang, X. Qin and P. Brault, *Materials Letters*, 2010, **64**, 115-118.
33. Y. Xu, D. Lin, X. Liu, Y. Luo, H. Xue, B. Huang, Q. Chen and Q. Qian, *ChemCatChem*, 2018, **10**, 2496-2504.
34. Y. Sun, X. Xiao, X. a. Dong, F. Dong and W. Zhang, *Chinese Journal of Catalysis*, 2017, **38**, 217-226.
35. Y. Sun, W. Han, F. Zhang, H. Li, Z. Zhang, X. Zhang, B. Shen, S.-Q. Guo and T. Ma, *Applied Catalysis B: Environmental*, 2024, **345**.
36. J. Toudert, R. Serna and M. Jiménez de Castro, *The Journal of Physical Chemistry C*, 2012, **116**, 20530-20539.
37. H. Wang, W. Zhang, X. Li, J. Li, W. Cen, Q. Li and F. Dong, *Applied Catalysis B: Environmental*, 2018, **225**, 218-227.
38. Z. Ni, W. Zhang, G. Jiang, X. Wang, Z. Lu, Y. Sun, X. Li, Y. Zhang and F. Dong, *Chinese Journal of Catalysis*, 2017, **38**, 1174-1183.
39. S. Xue, H. Deng, Q. Xie, Y. Hu, J. Yan, X. Zhao, F. Wang, Q. Zhang, L. Luo, C. Deng, C. He, D. Lin, S. Li, X. a. Wang and H. Luo, *Nanoscale*, 2019, **11**, 16928-16934.
40. C. Liang, H.-Y. Niu, H. Guo, C.-G. Niu, Y.-Y. Yang, H.-Y. Liu, W.-W. Tang and H.-P. Feng, *Chemical Engineering Journal*, 2021, **406**.
41. S. Weng, B. Chen, L. Xie, Z. Zheng and P. Liu, *Journal of Materials Chemistry A*, 2013, **1**.
42. N. Zhang, X. Li, H. Ye, S. Chen, H. Ju, D. Liu, Y. Lin, W. Ye, C. Wang, Q. Xu, J. Zhu, L. Song, J. Jiang and Y. Xiong, *J Am Chem Soc*, 2016, **138**, 8928-8935.
43. Y. Zang, S. Niu, Y. Wu, X. Zheng, J. Cai, J. Ye, Y. Xie, Y. Liu, J. Zhou, J. Zhu, X. Liu, G. Wang and Y. Qian, *Nat Commun*, 2019, **10**, 1217.
44. Q. Wang, Y. Lei, D. Wang and Y. Li, *Energy & Environmental Science*, 2019, **12**, 1730-1750.
45. X. Zhu, J. An, G. Chen, C. Xing, J. Bao and X. Xu, *Chemical Research in Chinese Universities*, 2023, **39**, 654-659.
46. Z. Li, B. Ma, X. Zhang, Y. Sang and H. Liu, *Environmental Research*, 2020, **182**.
47. W. Hou, J. Yang, H. Xu, D. Li, Z. Zou and D. Xia, *CrystEngComm*, 2020, **22**, 3956-3964.
48. C. Chen, T. Jiang, J. Hou, T. Zhang, G. Zhang, Y. Zhang and X. Wang, *Journal of Materials Science & Technology*, 2022, **114**, 240-248.
49. J. Yu, Z. Zheng, A. Wang, M. Humayun and Y. A. Attia, *Nanomaterials (Basel)*, 2024, **14**.

View Article Online
DOI: 10.1039/D5DT00940E

50. Y. Su, C. Li, X. Jiang and Y. Bai, *Inorganic Chemistry Communications*, 2025, **174**.
51. X. Zhang, X. Gu, Y. Song, R. Xie, S. Zhang, J. Li, S. Sheng and H. Zou, *Chemical Engineering Journal*, 2024, **495**.
52. Y. Gao, Y. Fu, J. Li, J. Duan, J. Li, Q. Mei and Q. Wang, *Journal of Alloys and Compounds*, 2024, **983**.
53. X. Liu, H. Cao and J. Yin, *Nano Research*, 2011, **4**, 470-482.
54. Z. Wang, S. Yan, Y. Sun, T. Xiong, F. Dong and W. Zhang, *Applied Catalysis B: Environmental*, 2017, **214**, 148-157.
55. C. X. Zhao, J. N. Liu, B. Q. Li, D. Ren, X. Chen, J. Yu and Q. Zhang, *Advanced Functional Materials*, 2020, **30**.
56. Q. Wang, Q. Ma, J. Lian, J. Zhong, F. Wang, J. Li, Y. He and R. Wang, *New Journal of Chemistry*, 2016, **40**, 5604-5610.
57. Y. Song, W. He, X. Sun, J. Lei, L. D. Nghiem, J. Duan, W. Liu, Y. Liu and Z. Cai, *Separation and Purification Technology*, 2023, **323**.
58. S. Wang, X. Zhang, S. Li, Y. Fang, L. Pan and J.-J. Zou, *Journal of Hazardous Materials*, 2017, **331**, 235-245.
59. J. Li, H. Yu, Y. Song, Z. Wei, F. Wang, X. Zhang, R. Xie and H. Zou, *Ceramics International*, 2023, **49**, 40676-40688.
60. M. Gao, D. Zhang, X. Pu, K. Ding, H. Li, T. Zhang and H. Ma, *Separation and Purification Technology*, 2015, **149**, 288-294.
61. Z. Zhao, Y. Cao, F. Dong, F. Wu, B. Li, Q. Zhang and Y. Zhou, *Nanoscale*, 2019, **11**, 6360-6367.
62. P. K. Ko and J. E. Halpert, *Chemical Research in Chinese Universities*, 2024, **40**, 556-560.
63. S. Wu, J. Xiong, J. Sun, Z. D. Hood, W. Zeng, Z. Yang, L. Gu, X. Zhang and S. Z. Yang, *ACS Appl Mater Interfaces*, 2017, **9**, 16620-16626.
64. P. Feng, X. Tang, J. Zhang, Y. Mei and H. Li, *RSC Advances*, 2017, **7**, 33241-33247.
65. W. Li, F. Xiao, H. Su, D. Wang and X. Yang, *RSC Advances*, 2016, **6**, 93309-93317.
66. X. Su, L. Hou, L. Xia, X. Yu, J. Guo, Y. Zhu and Y. Zhang, *Journal of Materials Science*, 2018, **54**, 4559-4572.
67. X. Ma, X. Tang, H. Yi, J. Cai and S. Q. Guo, *ChemistrySelect*, 2024, **9**.
68. J. Li, Y. Song, F. Wang, X. Zhang, H. Zhu and H. Zou, *Inorganic Chemistry Frontiers*, 2023, **10**, 4456-4470.
69. C. Chuaicham, S. Shenoy, J. Trakulmututa, V. Balakumar, P. Santawaja, S. Kudo, K. Sekar and K. Sasaki, *Separations*, 2023, **10**.

View Article Online
DOI: 10.1039/D5DT00940E

Data Availability Statement

The data that support the findings of this study are available on request from the corresponding authors.